Mon. Not. R. Astron. Soc. **000**, 000–000 (0000) Printed 5 February 2008 (MN LaTeX style file v2.2)

arXiv:astro-ph/0602175v1 8 Feb 2006

Simultaneous X-ray/optical observations of GX 9+9 (4U 1728–16)

A. K. H. Kong[1,6]⋆, P. A. Charles[2,5], L. Homer[3,6], E. Kuulkers[4] and D. O'Donoghue[5]

[1] *Kavli Institute for Astrophysics and Space Research, Massachusetts Institute of Technology,*
77 Massachusetts Avenue, Cambridge, MA 02139, U.S.A.
[2] *Department of Physics and Astronomy, University of Southampton, Southampton SO17 1BJ*
[3] *Astronomy Department, University of Washington, Box 351580, Seattle, WA 98195-1580, U.S.A.*
[4] *ISOC, ESA/ESAC, Urb. Villafranca del Castillo, P.O. Box 50727, 28080 Madrid, Spain*
[5] *South African Astronomical Observatory, PO Box 9, Observatory 7935, Cape Town, South Africa*
[6] *Department of Astrophysics, University of Oxford, Keble Road, Oxford OX1 3RH*

Accepted. Received.

ABSTRACT

We report on the results of the first simultaneous X-ray (*RXTE*) and optical (SAAO) observations of the luminous low mass X-ray binary (LMXB) GX 9+9 in 1999 August. The high-speed optical photometry revealed an orbital period of 4.1958 hr and confirmed previous observations, but with greater precision. No X-ray modulation was found at the orbital period. On shorter timescales, a possible 1.4-hr variability was found in the optical light curves which might be related to the mHz quasi-periodic oscillations seen in other LMXBs. We do not find any significant X-ray/optical correlation in the light curves. In X-rays, the colour-colour diagram and hardness-intensity diagram indicate that the source shows characteristics of an atoll source in the upper banana state, with a correlation between intensity and spectral hardness. Time-resolved X-ray spectroscopy suggests that two-component spectral models give a reasonable fit to the X-ray emission. Such models consist of a blackbody component which can be interpreted as the emission from an optically thick accretion disc or an optically thick boundary layer, and a hard Comptonized component for an extended corona.

Key words: accretion, accretion discs – binaries: close – stars: individual (GX 9+9) – X-rays: stars

1 INTRODUCTION

GX 9+9 (4U 1728–16) is a persistent bright galactic bulge X-ray source, with a 4.19 ± 0.02 hr orbital period that was reported by Hertz and Wood (1988) from *HEAO-1* data. The variations were roughly sinusoidal with an amplitude of 3.8%. However, there was clearly substantial scatter (4.6% residual error) about this modulation. The source showed a rich variety of X-ray variability on timescales from minutes to months and correlated X-ray spectra and fluxes (Mason et al. 1976; Parsignault & Grindlay 1978). Observations with *EXOSAT* show a spectrum and spectral variations very similar to GX 3+1, GX 13+1 and GX 9+1 (Schulz, Hasinger & Trümper 1989) and so GX 9+9 was classified as a high-luminosity atoll source (Hasinger & van der Klis 1989). The X-ray spectra obtained by *EXOSAT* and *Einstein* are very similar and can be represented by a blackbody of 1.5 keV and a thermal bremsstrahlung component of ~ 8 keV (Christian & Swank 1997). An *ASCA* observation revealed a similar kind of spectrum with a blackbody of ~ 1.3 keV plus a cutoff power law with photon index of ~ 1.2 and cutoff energy of ~ 6 keV (Church & Bałucińska-Church 2001). Line emission was also found from previous observations (*Einstein*: 0.77, 0.82 and 1.06 keV; Christian & Swank 1997; *ROSAT*: 0.65 and 0.97 keV; Schulz 1999) but a recent *ASCA* observation found none (Church & Bałucińska-Church 2001). An *RXTE* observation of GX 9+9 was carried out in 1996 but no kHz QPOs were found (Wijnands, van der Klis & van Paradijs 1998). There is no report of X-ray bursts from this source.

The optical counterpart ($V \sim 17$) is a 'Sco X-1-like' blue star with He II λ4686 and C III/N III λ4640 emission lines (Davidsen, Malina & Bowyer 1976; Charles, Thorstensen & Bowyer 1977). The only temporal study in the optical performed to date is that of Schaefer (1990) in which a $\sim 20\%$ modulation was present on the X-ray periodicity. There is no radio detection for GX 9+9 according to the recent Australia Telescope Compact Array observations at 4.8 and 8.64 GHz (Berendsen et al. 2000).

⋆ Email: akong@space.mit.edu

There have been no simultaneous optical/X-ray observations of this source so far. At $V = 17$ it is ideal for studying outer disc variability simultaneously with *RXTE* observations of the X-ray variability. In this paper, we report the results of the *first* simultaneous X-ray/optical observations of GX 9+9. An observation log for both X-ray and optical observations is presented in §2, while the temporal analysis of the data is in §3. In §4, time-resolved X-ray spectroscopy is presented and an archival study of X-ray modulation is reported in §5. The implications of our new data will be discussed in §6.

2 OBSERVATIONS

2.1 SAAO Observations

All optical observations were carried out with the UCT-CCD fast photometer (O'Donoghue 1995) at the Cassegrain focus of the 1.9-m telescope at the South African Astronomical Observatory (SAAO), Sutherland from 1999 August 11 to 14. The observing conditions were good with typical seeing of ∼ 1–2 arcsec and there was ∼ 6 hr observation time each night. In general, the seeing during the first two nights was quite stable while the image quality of the remaining two nights was relatively poor due to the variable seeing and high wind conditions. In order to achieve high time resolution, no filter was employed (i.e. white light) and a 5×5 on-chip prebinning was applied to maximise the time resolution. The timing resolution of all the data is 2 s. In Table 1, an observing log is presented together with the X-ray observations. Debiasing and flat-fielding were performed with standard IRAF routines. Since the star fields are crowded, differential photometry was obtained via PSF fitting with IRAF. The light curves of all four nights are shown in Fig. 1 to 4 and have typical error bars on individual 2 s observations of less than 2%.

Apart from the high-speed photometry, we also obtained a set of B and V images on 1999 August 15. The exposure times on GX 9+9 were 60 s in the B-band and 40 s in the V-band. We calibrated the magnitudes using a photometric standard, giving $B = 16.96 \pm 0.05$ and $V = 16.79 \pm 0.05$.

2.2 *RXTE* Observations

GX 9+9 was observed with the Proportional Counter Array (PCA) instrument on board the *RXTE* (Bradt, Rothschild & Swank 1993) between 1999 August 11 and August 14 (see Table 1). The PCA consists of five identical Proportional Counter Units (PCUs) sensitive to X-rays with an energy range of 2–60 keV and a total effective area of ~ 6500 cm^2. The PCA spectral resolution at 6 keV is approximately 18 per cent, and the maximum timing resolution available is 1 μs. Three PCUs were on during our observations. For most of the time, *RXTE* observed the source simultaneously with the optical telescope at SAAO. The typical on-source time for each night is about 10–14 ks (see Table 1). Apart from the standard configuration of the PCUs (Standard1 and Standard2 modes which are always available), we also employed event modes with maximum timing resolution of 125 μs and 64 spectral energy channels in order to maximise the timing and spectral resolution. All X-ray spectra presented here have been corrected for background and dead-time with FTOOLS v4.2 and Epoch 4 PCA background model.

Table 1. A Journal of the X-ray/optical observations of GX 9+9.

Observatory	Detector	Date	Time (UT)	
			Start	End
SAAO	1.9m +	1999 August 11	17:26	23:08
	UCT CCD	1999 August 12	17:15	23:08
		1999 August 13	17:16	23:00
		1999 August 14	17:45	23:05
RXTE	PCA	1999 August 11	17:20	00:06
		1999 August 12	17:28	00:03
		1999 August 13	17:27	22:41
		1999 August 14	17:26	22:40

3 TIMING ANALYSIS

3.1 Optical

It is very clear from Figs. 1 to 4 that substantial variability is present in the optical light curves of GX 9+9. In order to search for any modulation in the light curves, we used the Lomb-Scargle periodogram (Lomb 1976; Scargle 1982; hereafter LSP), a modification of the discrete Fourier transform which is generalised to the case of uneven spacing. We have also employed Phase Dispersion Minimisation (PDM; Stellingwerf 1978) to check the results from LSP, as PDM is more sensitive to non-sinusoidal modulation. Before performing period-searching, the light curves were normalised to fractional count rate in order to eliminate nightly variations. All the light curves were then combined into a single dataset which was used to calculate the LSP. Fig. 5 shows the LSP of the combined light curve and there is a very strong peak at 4.1958 ± 0.0005 hr. Also present in the LSP are the aliases from this modulation. This is demonstrated by applying the LSP to a simulated light curve of a pure sinusoidal modulation at 4.1958 hr and with the same time sampling as the real data (see Fig. 5). This shows how the LSP ought to appear if there were only a 4.1958 hr modulation in the data. The principal features of the LSP are restored when comparing with the real data. A folded light curve on the 4.1958 hr modulation is shown in Fig. 5 in which the phase zero is set at the time of the first data point (HJD 2451402.23164) and it is highly sinusoidal with semi-amplitude of 9.8%. Figure 6 shows the nightly folded light curves on the 4.1958 hr modulation and the sinusodial modulation is very stable. It is worth noting that the phase zero roughly corresponds to minimum light as determined from the data. A PDM analysis was also performed which confirmed these results. The LSP of several check stars with similar brightness as the target star were also calculated but none of these show any modulation at 4.1958 hr, with an upper limit of semi-amplitude ∼ 0.17% . Such small scale variations are mainly due to the local atmospheric transparency variations commonly found at SAAO (e.g. Homer, Charles & O'Donoghue 1998). The combined results indicate that the highly sinusoidal and significant modulation at 4.1958 hr of GX 9+9 represents the intrinsic behaviour of

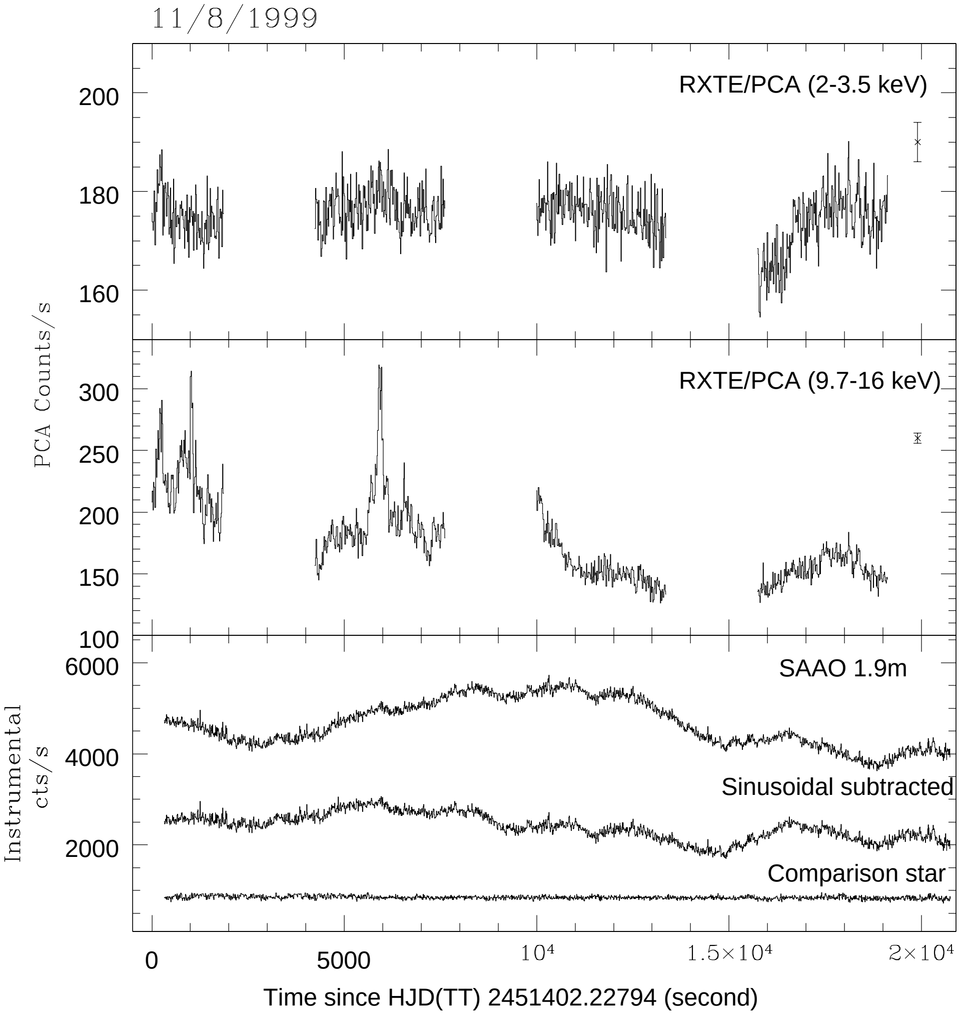

Figure 1. Simultaneous X-ray and optical light curves of GX 9+9 on 11/8/99. The X-ray light curve was divided into two energy bands: 2–3.5 keV (upper panel) and 9.7–16 keV (middle panel); typical error bars for the X-ray data are also shown. The timing resolution is 16 s for X-ray data and 2 s for optical data. For clarity, the optical light curve (lower panel) has been rebinned to 10 s. Note that a 4.2-hr orbital modulation is obvious in the optical light curve. Also shown underneath the source is a light curve with the 4.2-hr sinusoidal modulation subtracted. Optical light curves of a comparison star are also plotted.

the source and is entirely consistent with the previously reported orbital period (Schaefer 1990) but to a greater degree of accuracy.

For modulation on shorter timescales ($\sim$ 1000 s), we expect any sub-orbital modulation which is either periodic, or quasi-periodic will be evident in the LSP or PDM of the data, and should repeat from night to night. Therefore the LSP and PDM for each night were calculated in order to search for such variability. Before calculating both the LSP and PDM, the 4.19-hr orbital modulation was subtracted (assuming a sinusoid at this period; see Fig. 1 to 4). In Fig. 7, the nightly LSP is shown together with the 99% confidence level in both white noise (Gaussian noise) and red noise. It is apparent that in Fig. 7 those peaks between 0.5–1 hr^{-1} are below the red-noise level. From the log-log binned power density spectrum (PDS; insets of Fig. 7), both the actual and simulated PDS are similar, indicating the variability of the source on short timescales can be described as the combination of white and red noise. All the PDS level off at high frequency ($\sim$ 30 hr^{-1}), suggesting that white noise becomes dominant between 30 and 900 hr^{-1} (the Nyquist frequency). There is also an indication that an excess appears at $\sim$ 1.4 hr from the log-log PDS. In determining the white-noise confidence level, we generate Gaussian noise datasets with the same time intervals and variance as the true data and then perform the LSP analysis on the resulting datasets. The peak power in each periodogram (which must be purely due to noise) was then recorded. This was repeated 10,000 times for good statistics. However, the noise is not necessarily Gaussian, and can also be frequency dependent with a higher power at lower frequencies. By using the above method, strong peaks at the low frequencies might give misleading results. In order to take into account such a noise contribution in the data, we simulate the noise in the form of a power law, which is also known as red noise (e.g. Done et al. 1992). Quantitatively, the power spectrum of the

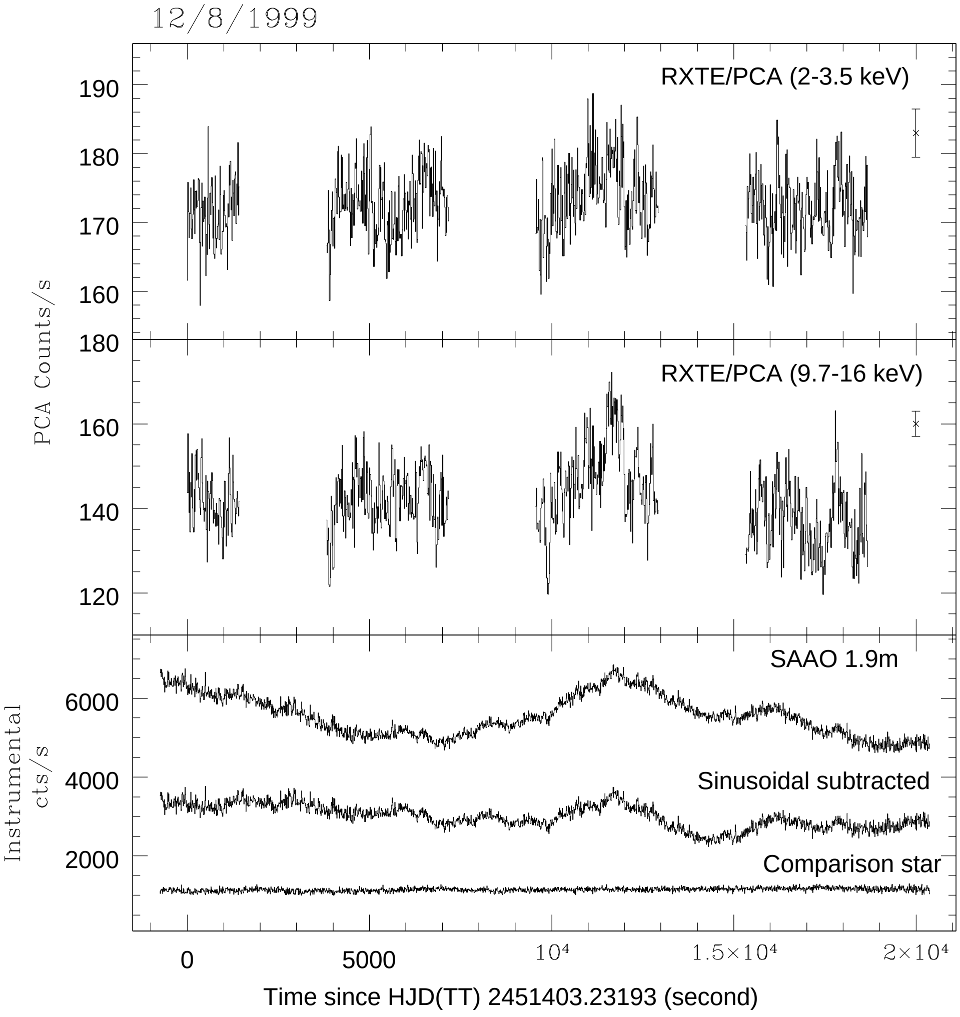

Figure 2. Same as Fig. 1, but for 12/8/99.

"red-noise" light curve will be given by $(1/\omega)^\alpha$, where ω is frequency and α is the slope index. Following an implementation of the method of Timmer & König (1995), we generate the simulated light curve with a red-noise power spectrum, together with the same time sampling and variance as the original data. Finally, we combine the white-noise simulated light curve as mentioned above, with the red-noise simulated light curve, by scaling the data points in each such that the relative contribution of both white and red-noise components is as specified. Following the method used previously to determine the white-noise confidence level, we derive the red-noise confidence level with the combined simulated light curve. Since red noise is frequency dependent, we need to compute the confidence level for a set of frequency bins. Hence it looks like a histogram rather than a horizontal line as for the white-noise level (see Fig. 7). Note that the peak at around 1.4 hr (0.7 hr^{-1}) is just below the red-noise level in the first night yet it seems to repeat itself in other nights, demonstrating its quasi-periodic nature. Hence, the negative result from the LSP suggests that such variabilities are not strictly periodic, but are due to some form of quasi-periodic behaviour. The 1.4-hr variability may be an intrinsic property of the source and it may be associated with the mHz QPOs which were also found in other LMXBs (e.g. Chakrabarty et al. 2001).

3.2 *RXTE*

A similar temporal analysis was performed for the *RXTE* data. In order to study the variability in different energy bands, light curves from two energy ranges (2–3.5 keV and 9.7–16 keV) were extracted for each night. From Fig. 1–4, it is clear that flaring is stronger at higher energies. In soft X-rays, the count rate roughly remains at a constant level, while the flares in hard X-rays can be by a factor of ~ 2. The LSP and PDM were calculated from the combined 2–16 keV band pass, as in the case of the optical data. The PDM method is particularly important for the X-ray data since the source changed its spectral state from time to time (see §4 for details about the spectral behaviour of the source) and therefore any modulation would be expected to be non-sinusoidal. Fig. 8 shows the resulting LSP and PDM for the

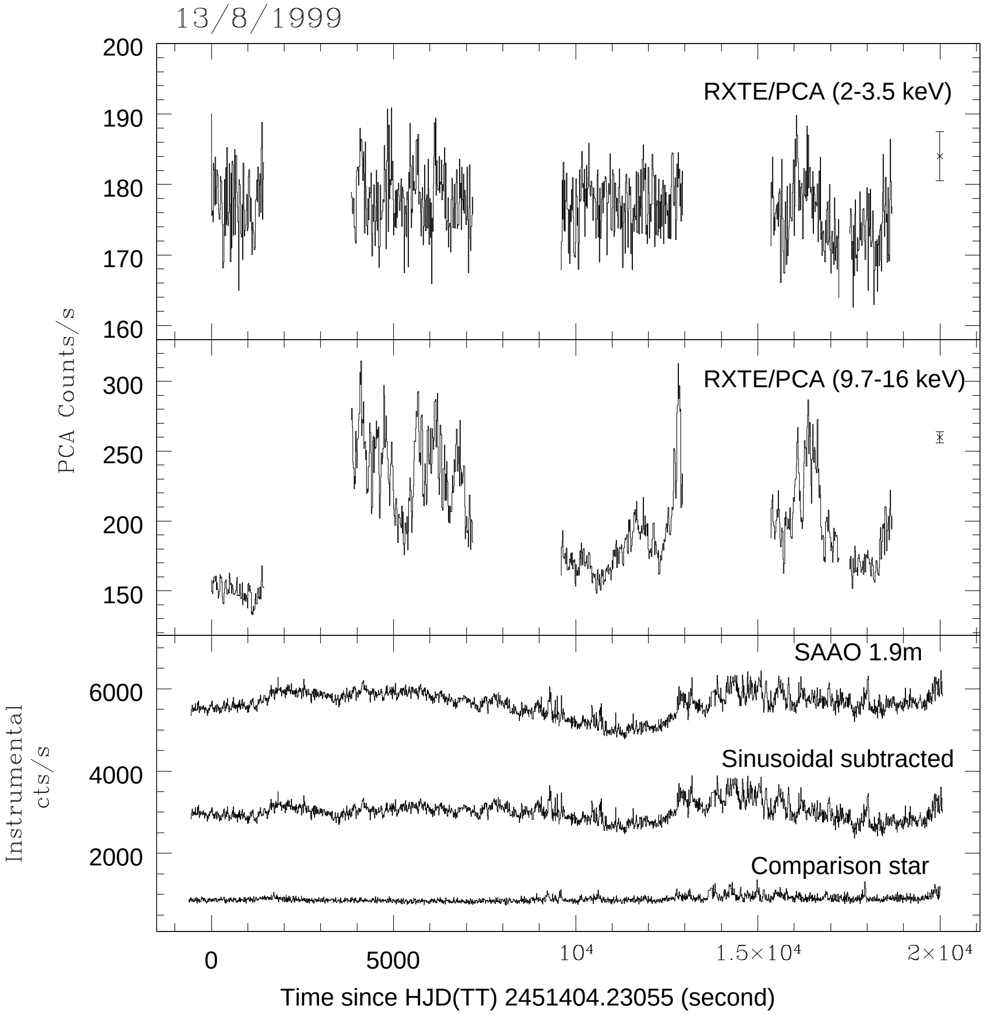

Figure 3. Same as Fig. 1, but for 13/8/99.

2–3.5 keV *RXTE* data. There is no distinct peak at the optical periodicity of 4.19 hr (marked) and hence the 4.19-hr X-ray modulation is below the detection threshold in our observations. At the 3-σ confidence level, upper limits of 0.9% and 6.7% can be set for the semi-amplitude of any 4.19-hr variability in the 2–3.5 keV and 9.7–16 keV bands respectively. The 3.8% amplitude seen in *HEAO-1* data is below the hard X-ray detection threshold and it is not implausible that a weaker signal is present. Note that the sudden jump at about 0.6–0.9 hr^{-1} in the 99% red noise confidence level is due to the window function arising from the data gaps, typically seen in low-Earth orbit satellites. Since the red noise is frequency dependent, the confidence level will be different for different frequency bins and therefore such analysis also reflects the window function (if it exists) in the data.

Variability on shorter timescales is also seen in the LSP but it is not significant. A period analysis for each night was also performed and the resulting LSPs are shown in Fig. 9. There is no significant peak at the 4.19-hr orbital period which confirms the result from the combined light curves. On shorter timescales, those marginally significant peaks do not repeat more than one night and they are also comparable to the observing windows of the spacecraft orbit, typically $\lesssim$1 hr due to SAA passages. Hence they are not considered further.

The X-ray PDS of GX 9+9 was also calculated for each night in order to search for kHz QPOs. The PDS was derived from the 125 μs time resolution data over 100–4000 Hz. However, the analysis resulted in a negative finding and an upper limit (95% confidence) was set of 1.6% to the rms amplitude of QPOs with a FWHM of 150 Hz (in 2–60 keV).

3.3 Comparison of Light Curves

The simultaneous X-ray/optical light curves (Fig. 1–4) exhibit complex variability and it is interesting to look for any correlation. We first applied cross-correlation analysis to compare the sinusoidal subtracted optical light curves with the X-ray light curves in different energy bands. We also divided the light curves into smaller intervals to study the cross-correlation. We repeated this analysis for all four

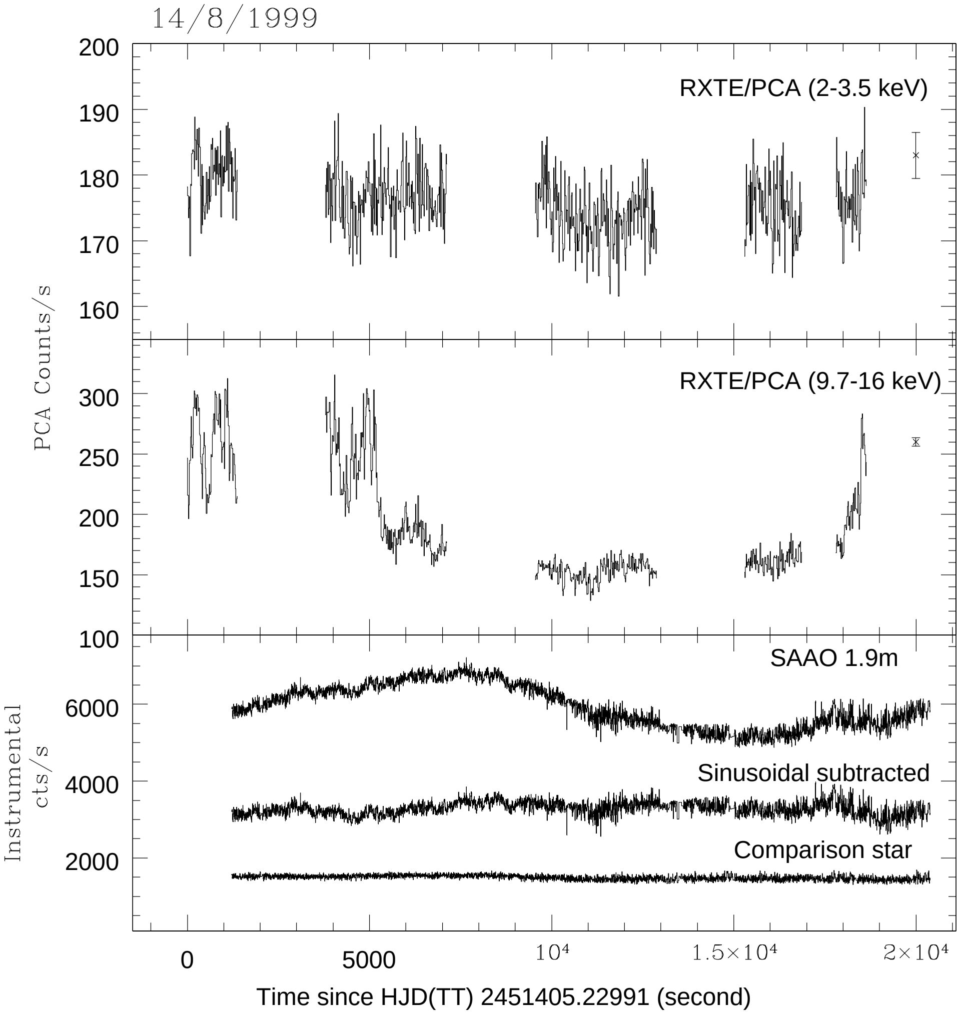

Figure 4. Same as Fig. 1, but for 14/8/99.

observations. There is no significant correlation indicating that the correlated response is very weak. Fig. 10 shows a close up of the light curves from Fig. 1, in which there is a prominent X-ray flare in the second *RXTE* visit. However, there is no immediate response in the optical. Similar uncorrelated variability can also be found from other light curves. We have tried to use the transfer function technique as employed by Kong et al. (2000) to investigate the correlations, but the optical light curves could not be reproduced as a convolution of the X-ray light curve with a Gaussian transfer function. Hence this suggests that the optical emission does not significantly respond to X-ray variability. We note, however, that the presence of uncorrelated events does not imply the absence of correlated ones.

4 X-RAY SPECTROSCOPY

Colour-colour (CD) and hardness-intensity diagrams (HID) were derived from the same four energy bands as used by Wijnands, van der Klis & van Paradijs (1998) to facilitate comparison: 2–3.5, 3.5–6.4, 6.4–9.7 and 9.7–16 keV. The soft and hard colours are defined as the count rate ratio between 3.5–6.4 keV and 2–3.5 keV and between 9.7–16 keV and 6.4–9.7 keV, respectively. The total intensity for the HID was taken as the sum of the total count rates (1 PCU) in the same energy bands as were used in calculating the colours. All the data were binned to a time resolution of 64 seconds. The CD and HID of all the X-ray data are shown in Fig. 11. Both the CD and HID of GX 9+9 suggest that the source was on the banana branch (Hasinger & van der Klis 1989) during the *RXTE* observations. Both diagrams show very clear correlation and this is typical for GX 9+9 (see e.g. Schulz, Hasinger & Trümper 1989; Wijnands, van der Klis & van der Paradijs 1998).

As there is clear indication of correlation between intensity and colour ratio from the CD and HID, correlated spectral parameters and intensity are expected, therefore 24 approximately half-hour summed spectra were derived from the light curves (see Table 2) for further spectral fitting. Based on the spectral analysis of archival Crab Nebula and pulsar data (e.g. Dove et al. 1998; Wilms et al. 1999; Bloser et al. 2000a; Barret et al. 2000; Kong 2000), we restrict our

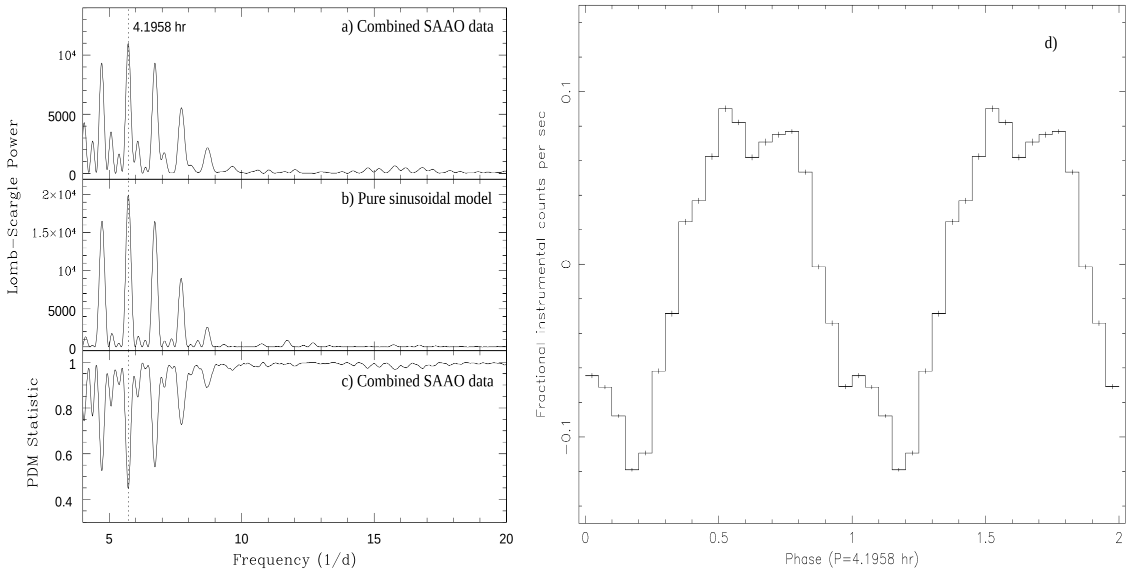

Figure 5. LSP and PDM analysis of the combined SAAO data (left): a) LSP of GX 9+9 data; b) Pure sinusoidal at 4.1958 hr and c) PDM of GX 9+9 data. Right: Folded optical light curve of GX 9+9 on a period of 4.1958 hr. Two cycles are shown for clarity. Phase zero is arbitrarily set at the time of the first data point (HJD 2451402.23164).

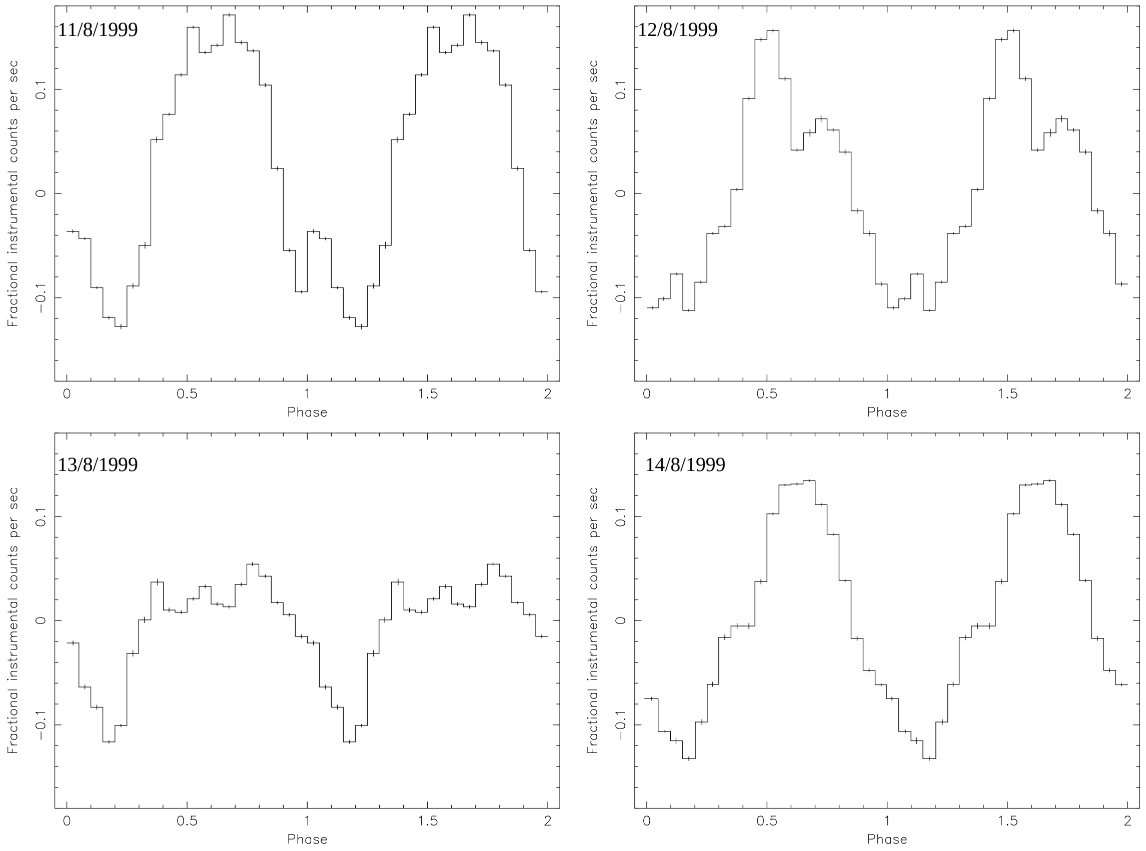

Figure 6. Nightly folded optical light curve of GX 9+9 on a period of 4.1958 hr. Two cycles are shown for clarity. Phase zero is arbitrarily set at the time of the first data point (HJD 2451402.23164). The relatively smaller amplitude of the August 13, 1999 data is due to the bad seeing near the end of the run (see also Figure 3).

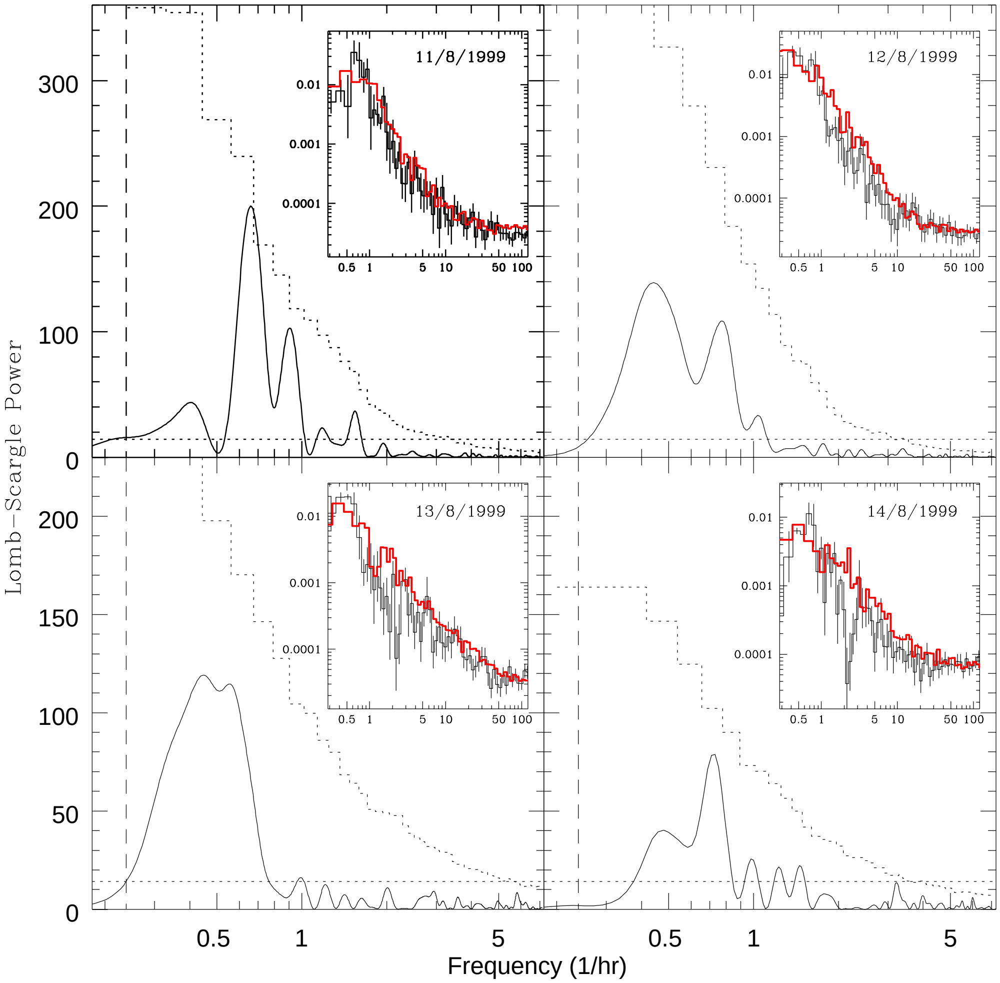

Figure 7. LSP of GX 9+9 after subtracting the 4.19-hr sinusoidal modulation. The dotted horizontal line is the 99% confidence level assuming white noise, while the dotted histogram is the 99% confidence level due to red noise. The 4.19-hr orbital period is marked by a vertical dashed line. Insets: the log-log binned power density spectra (with error bars), with the average of 200 simulated white-noise plus red-noise models over-plotted (thick line). Note that the power spectra level off at high frequency due to the large contribution of white noise.

spectral analysis to the energy range of 2.5–20 keV, outside which the calibration is not reliable. In addition, a 1% systematic error was added to account for the uncertainty of the calibration before the spectral fitting.

Previous attempts to fit the X-ray energy spectrum of GX 9+9 show that it cannot be fitted well with a single-component model (either power law, blackbody, cutoff power law or thermal bremsstrahlung; e.g. Schulz 1999). These single-component models were fitted first to our *RXTE* data but the results were similarly negative with unacceptable χ^2_ν (> 2). Two-component models were then applied to the spectra. Combinations of blackbody plus cutoff power law (BB+CPL), blackbody plus thermal bremsstrahlung (BB+TB), and blackbody plus Comptonization (BB+CompST; Sunyaev & Titarchuk 1980 and BB+CompTT; Titarchuk 1994) result in a significant improvement to the spectral fits (see Tables 2–5 and Fig. 12). All models included a column density N_H, which was kept fixed at 2.1×10^{21} cm^{-2} (e.g. Church & Bałucińska-Church 2001) for all the fits since it tended to vary over a wide range if left as a free parameter. We also note that from an optical spectroscopic observation (Shahbaz et al. 1996), the interstellar absorption features suggest a reddening of $E(B-V) = 0.1 - 0.4$. Hence, the column density can be derived by using the conversion of $N_H/10^{22}\mathrm{cm}^{-2} = 0.179 A_V$ (Predehl & Schmitt 1995) and $A_V = 3.1E(B-V)$ (Schild 1977), suggesting N_H is in the range of $0.6 - 2.2 \times 10^{21}$ cm^{-2}. The total flux of GX 9+9 varies between 6.8–8.9 $\times 10^{-9}$ erg cm^{-2} s^{-1}, corresponding to $2 - 2.7 \times 10^{37} D_5^2$ erg s^{-1} where D_5 is in units of 5 kpc (e.g. Church & Bałucińska-Church 2001) over the four days of our observations. The best-fit parameters of all the models for the 24 spectra are given in Tables 2–5. The effective radius of the blackbody emitting surface R_{bb} and the ratio of the blackbody flux to the total flux in the 2–20 keV band, F_{bb}/F_{total} are also included. For the BB+CompST and BB+CompTT models, the Comptonizing

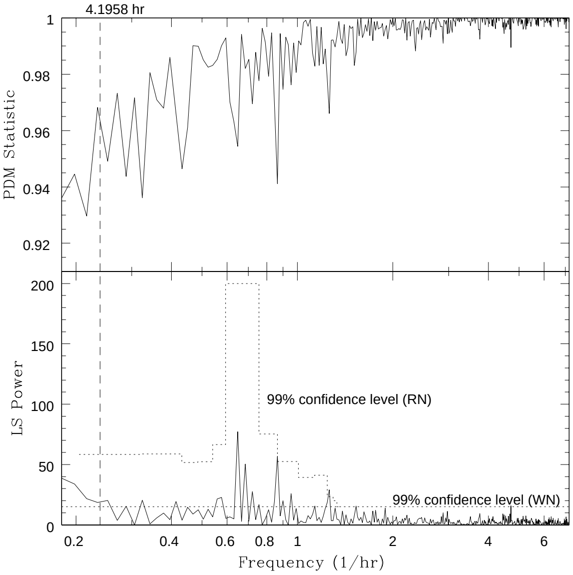

Figure 8. LSP and PDM analysis of the combined *RXTE* data in the 2–3.5 keV band. The horizontal dotted line is the 99% confidence level from white noise (WN), while the dotted histogram is the 99% confidence level due to red noise (RN). Note that the sudden jump in the red noise confidence level is due to the window function of the data.

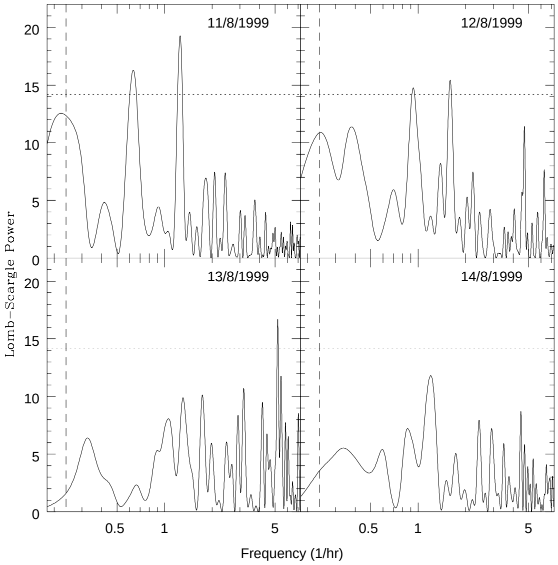

Figure 9. LSP of the nightly *RXTE* data in 2–3.5 keV. The dotted horizontal line is the 99% confidence level from white noise, while the vertical dashed line is the 4.19-hr orbital period.

y-parameter, defined as $y = 4kT_e\tau^2/m_ec^2$ was derived. In Fig. 12, the spectral parameters of all the models are plotted as a function of the total (2–20 keV) flux. For all the models, the blackbody temperature is about 1.4–2 keV and is always correlated with the total flux. As the total flux increases, the blackbody component increases from $\sim$ 10% to 40% while the other component remains roughly constant. Hence, the increase of the blackbody emission may also be responsible to the flaring activities. Such positive correlation also reflects the correlation between the intensity level and the hardness ratios described in the HID. The blackbody radius R_{bb} drops slightly from $\sim$ 2.5 km to $\sim$ 2 km when the total flux increases.

For the BB+CPL model, the photon index is roughly at $\sim$ 1.6 with no indication of any correlation with the total flux. Meanwhile, the cutoff energy E_{cut} varies from 5.5 keV to 7 keV. Such results indicate that the contribution of the CPL component remains roughly constant as the total flux increases, while the BB component becomes the major driving force for the spectral evolution of the source. For the

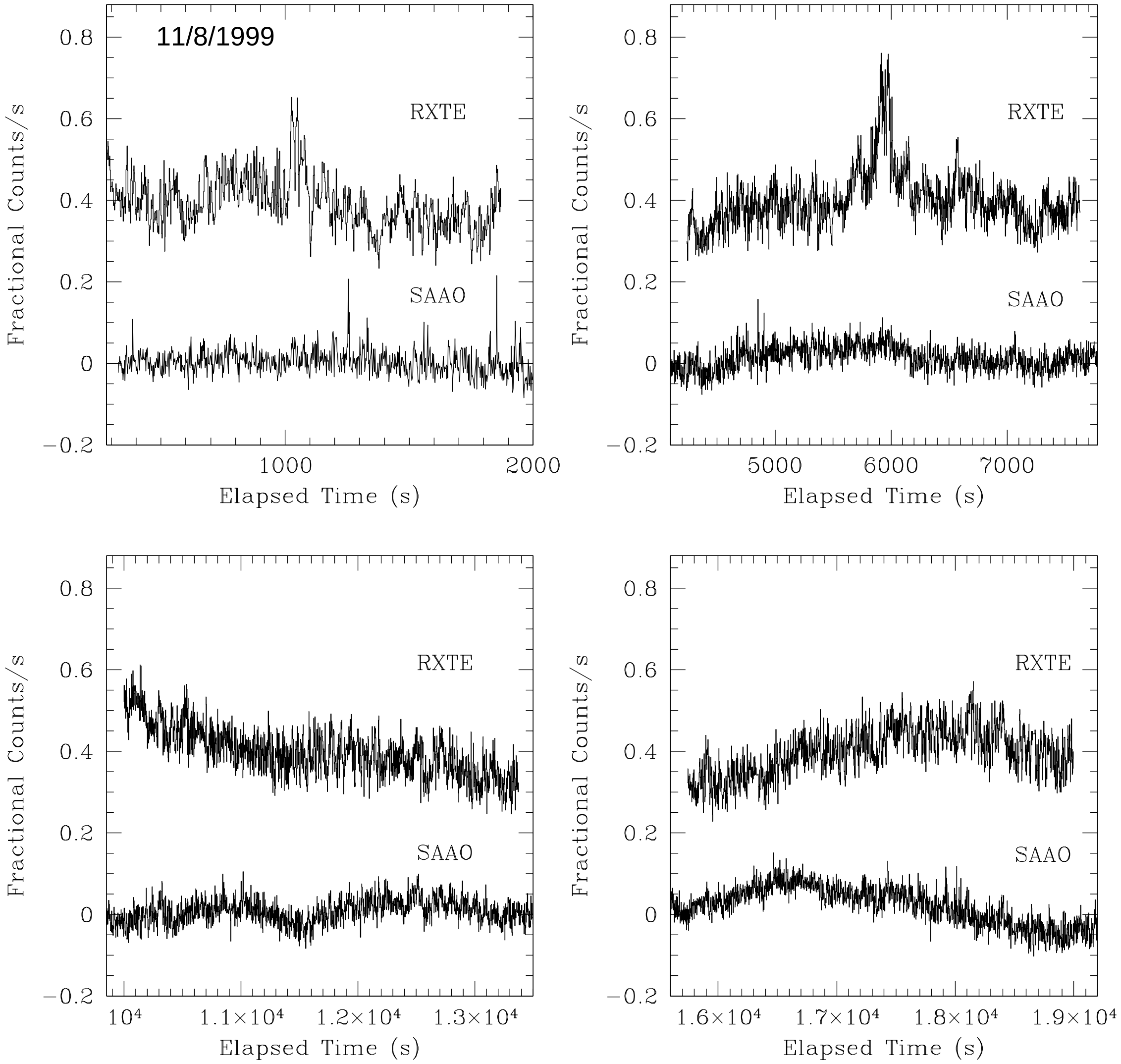

Figure 10. A close up of the simultaneous X-ray and optical (sinusoidal subtracted) light curves of GX 9+9 on 11/8/99. The timing resolution is 1.875 s for X-ray data and 2 s for optical data. The count rate for both datasets is normalised to fractional count rate.

BB+TB model, the thermal bremsstrahlung temperature varies from 5 keV to 6 keV and is correlated with the total flux.

For the BB+CompST, the optical depth τ is moderate at about 9–12 and might be roughly anti-correlated with the blackbody contribution. The electron temperature is very steady at $\sim$ 3 keV although small variations can be seen and are also anti-correlated with the optical depth. The BB+CompTT results are very similar to BB+CompST but with larger error bars in τ and kT_e. The additional parameter in CompTT, the seed photon temperature (T_0), is steady at $\sim$ 0.5 keV. Also τ in CompTT is slightly smaller than that of the CompST while kT_e is larger than that of the CompST.

We also investigate the effect of replacing the BB component with a multi-colour disc blackbody model (DBB; Mitsuda et al. 1984) in all models. All the fits were acceptable but resulted in a large colour temperature for the inner disc ($kT_{in} \gtrsim 3$ keV) and an unfeasibly small inner disc radius ($R_{in} = 1$ km). The error bars for the other component (i.e. CPL, CompST and CompTT) were also large compared to the BB models. Therefore the DBB model seems to be unrealistic.

5 ARCHIVAL X-RAY OBSERVATIONS

If the 4.19-hr modulation is orbital in nature, it should be very stable (as in the optical). In order to study the X-ray modulation on this timescale, light curves from the public data archives were obtained and only observations longer than 15 ks ($\gtrsim$ 4.2 hr) were considered. Table 6 shows all the relevant observations with the date and duration of the observations. An $\sim$ 17.4-hr nearly uninterrupted *EXOSAT* observation and an $\sim$ 13-hr *ASCA* observation were extracted

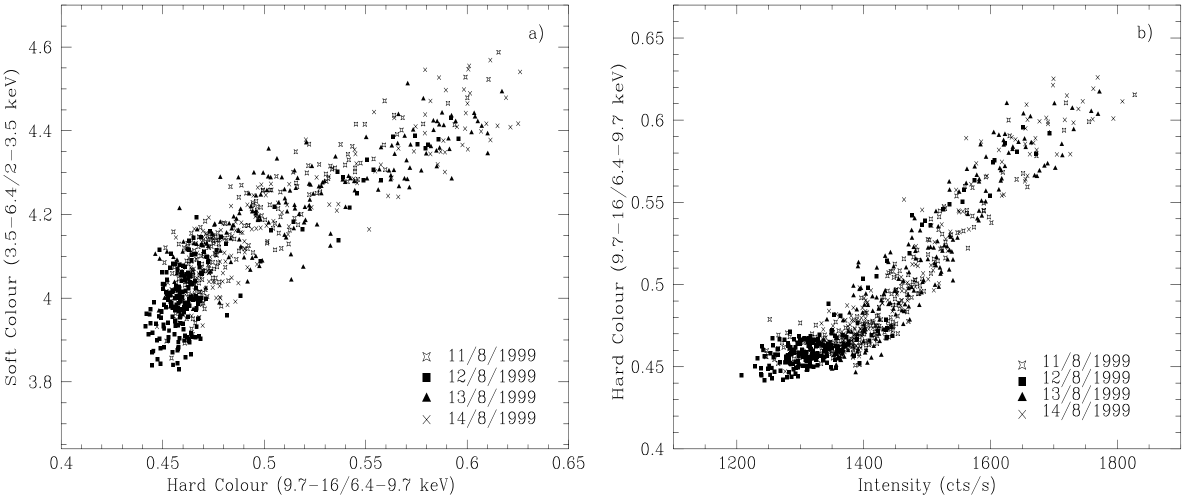

Figure 11. The colour-colour diagram (a) and hardness-intensity diagram (b) of all four nights data of GX 9+9. Each data point is an accumulation of 64 s.

Table 2. Spectral fits of GX 9+9 with the BB+CPL model.

Number	Start (UT)	End (UT)	Γ^a	E^b_{cut} (keV)	kT^c_{bb} (keV)	F^d_{tot}	F_{bb}/F^e_{tot}	R^f_{bb} (km)	χ^2_ν (34 dof)
1	11 17:22:23	17:55:59	1.43 ± 0.07	5.85 ± 0.39	2.04 ± 0.04	8.3	0.23	1.61 ± 0.06	0.68
2	11 18:29:03	18:54:19	1.59 ± 0.10	6.41 ± 0.58	1.69 ± 0.02	7.61	0.21	2.12 ± 0.05	0.88
3	11 19:02:23	19:35:59	1.44 ± 0.08	5.60 ± 0.38	1.88 ± 0.04	7.82	0.20	1.69 ± 0.07	0.67
4	11 20:25:43	21:15:59	1.65 ± 0.08	6.13 ± 0.41	1.59 ± 0.02	7.08	0.18	2.14 ± 0.05	1.08
5	11 21:15:59	22:39:19	1.66 ± 0.07	6.48 ± 0.39	1.58 ± 0.01	7.11	0.21	2.31 ± 0.03	0.60
6	11 23:12:23	23:45:59	1.71 ± 0.10	6.68 ± 0.59	1.63 ± 0.02	7.41	0.21	2.27 ± 0.06	0.91
7	12 14:28:15	18:01:51	1.65 ± 0.10	6.10 ± 0.53	1.57 ± 0.02	6.89	0.16	2.07 ± 0.05	0.77
8	12 18:34:55	19:25:11	1.64 ± 0.07	6.06 ± 0.35	1.58 ± 0.02	6.95	0.16	2.00 ± 0.05	0.68
9	12 19:58:15	20:31:51	1.61 ± 0.10	5.93 ± 0.49	1.58 ± 0.03	6.90	0.14	1.90 ± 0.07	0.88
10	12 20:31:52	21:05:11	1.60 ± 0.09	5.97 ± 0.43	1.59 ± 0.02	7.12	0.18	2.13 ± 0.05	0.91
11	12 21:38:15	22:45:11	1.53 ± 0.07	5.56 ± 0.29	1.55 ± 0.02	6.76	0.13	1.86 ± 0.05	0.79
12	13 17:26:23	17:59:59	1.64 ± 0.10	6.09 ± 0.52	1.56 ± 0.02	7.19	0.19	2.34 ± 0.06	1.01
13	13 18:16:23	18:49:59	1.42 ± 0.09	5.48 ± 0.57	2.26 ± 0.07	8.77	0.28	1.47 ± 0.09	0.87
14	13 18:50:00	19:39:59	1.53 ± 0.07	6.31 ± 0.41	2.05 ± 0.04	8.42	0.25	1.65 ± 0.06	0.5
15	13 19:56:23	20:29:59	1.59 ± 0.10	6.11 ± 0.51	1.68 ± 0.03	7.44	0.20	2.07 ± 0.07	0.86
16	13 20:29:59	20:54:59	1.61 ± 0.10	6.46 ± 0.55	1.73 ± 0.02	7.80	0.24	2.19 ± 0.05	1.21
17	13 21:36:23	22:09:59	1.52 ± 0.08	6.16 ± 0.45	1.97 ± 0.04	8.16	0.24	1.74 ± 0.07	0.86
18	13 22:09:59	23:00:00	1.77 ± 0.10	7.56 ± 0.75	1.72 ± 0.02	7.56	0.24	2.21 ± 0.05	1.07
19	14 17:25:35	17:59:11	1.60 ± 0.09	7.07 ± 0.63	2.05 ± 0.04	8.93	0.29	1.85 ± 0.07	0.82
20	14 18:23:55	18:50:51	1.55 ± 0.08	6.76 ± 0.60	2.14 ± 0.04	8.75	0.27	1.60 ± 0.06	0.78
21	14 18:57:15	19:39:11	1.60 ± 0.09	6.39 ± 0.51	1.72 ± 0.02	7.67	0.22	2.10 ± 0.05	0.64
22	14 19:55:35	21:02:31	1.73 ± 0.07	6.76 ± 0.42	1.60 ± 0.01	7.15	0.21	2.31 ± 0.03	0.7
23	14 21:35:35	22:09:11	1.61 ± 0.10	6.55 ± 0.56	1.58 ± 0.02	7.29	0.19	2.28 ± 0.06	0.9
24	14 22:17:15	22:42:31	1.58 ± 0.10	6.82 ± 0.74	1.89 ± 0.05	8.00	0.21	1.75 ± 0.09	0.93

[a] Photon index
[b] Cutoff energy
[c] Blackbody temperature
[d] Total flux in 2–20 keV ($10^{-9}\,\mathrm{erg\,cm^{-2}\,s^{-1}}$)
[e] Ratio of blackbody flux to total flux, 2–20 keV
[f] Blackbody radius, assuming a distance of 5 kpc

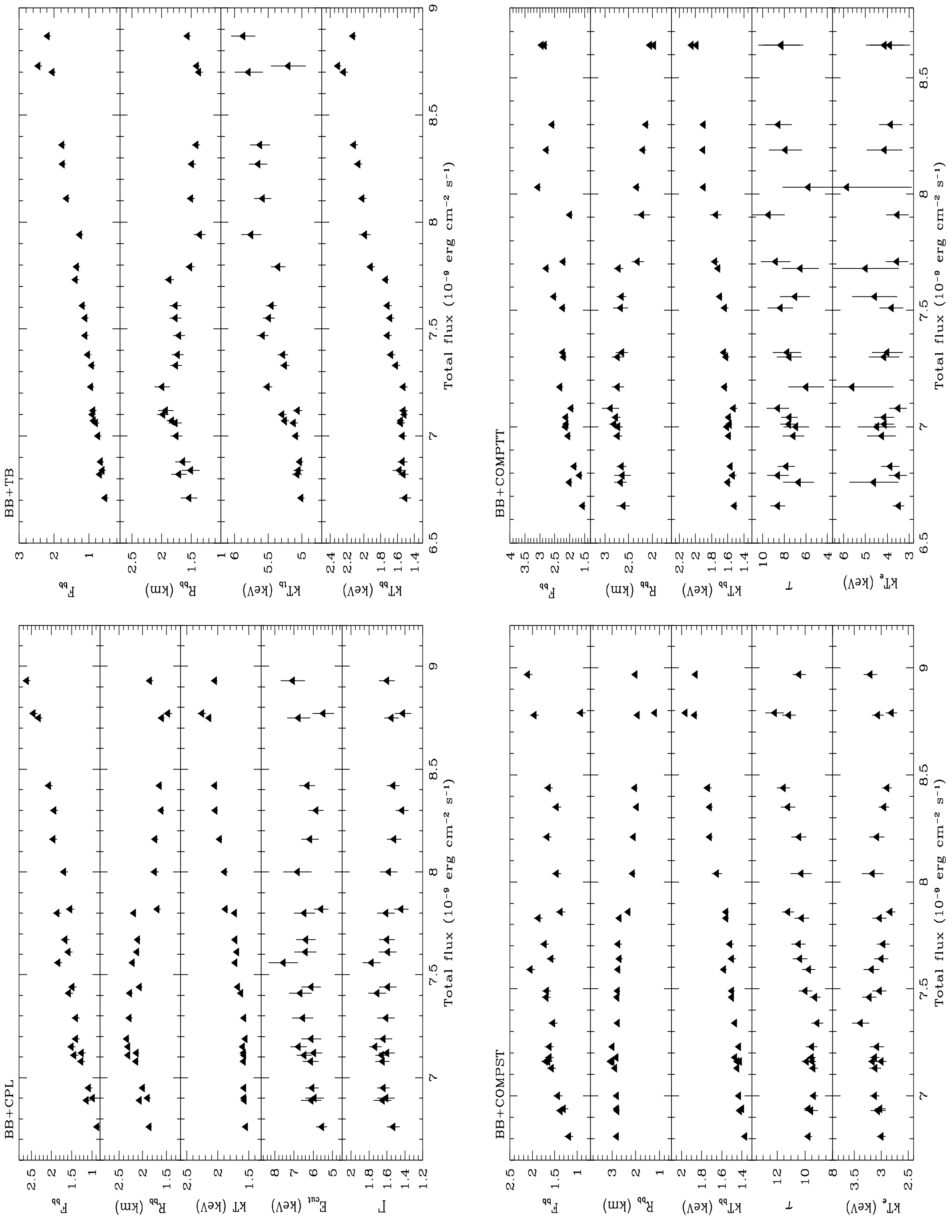

Figure 12. Variation of spectral parameters for the BB+PL, BB+TB, BB+CompST and BB+CompTT models with the total flux in 2–20 keV.

Table 3. Spectral fits of GX 9+9 with the BB+TB model.

Number	kT_{bb} (keV)	kT^a_{tb} (keV)	F_{tot}	F_{bb}/F_{tot}	R_{bb} (km)	χ^2_ν (35 dof)
1	2.07 ± 0.05	5.65 ± 0.14	8.27	0.21	1.49 ± 0.07	0.69
2	1.69 ± 0.05	5.49 ± 0.09	7.55	0.15	1.77 ± 0.10	0.92
3	1.92 ± 0.05	5.35 ± 0.11	7.79	0.17	1.52 ± 0.08	0.66
4	1.54 ± 0.05	5.09 ± 0.06	7.00	0.11	1.75 ± 0.10	1.25
5	1.52 ± 0.04	5.29 ± 0.06	7.10	0.13	1.98 ± 0.10	0.72
6	1.62 ± 0.05	5.25 ± 0.07	7.33	0.13	1.76 ± 0.10	1.06
7	1.53 ± 0.06	5.07 ± 0.07	6.82	0.10	1.71 ± 0.13	0.90
8	1.54 ± 0.06	5.03 ± 0.05	6.88	0.10	1.64 ± 0.13	0.80
9	1.58 ± 0.08	5.05 ± 0.07	6.84	0.09	1.51 ± 0.15	0.92
10	1.56 ± 0.05	5.12 ± 0.06	7.06	0.11	1.77 ± 0.11	1.06
11	1.51 ± 0.07	5.01 ± 0.05	6.71	0.08	1.54 ± 0.14	0.84
12	1.53 ± 0.05	5.06 ± 0.07	7.12	0.12	1.93 ± 0.13	1.11
13	2.31 ± 0.04	5.20 ± 0.26	8.73	0.28	1.41 ± 0.05	0.83
14	2.12 ± 0.05	5.62 ± 0.15	8.36	0.21	1.42 ± 0.07	0.58
15	1.68 ± 0.05	5.28 ± 0.08	7.38	0.14	1.73 ± 0.10	0.95
16	1.74 ± 0.04	4.48 ± 0.09	7.73	0.18	1.87 ± 0.08	1.30
17	2.02 ± 0.05	5.58 ± 0.13	8.11	0.20	1.51 ± 0.07	0.91
18	1.72 ± 0.05	5.58 ± 0.09	7.47	0.15	1.71 ± 0.10	1.42
19	2.13 ± 0.04	5.87 ± 0.18	8.87	0.25	1.57 ± 0.06	0.92
20	2.24 ± 0.05	5.79 ± 0.21	8.70	0.24	1.37 ± 0.06	0.86
21	1.72 ± 0.05	5.45 ± 0.08	7.61	0.16	1.77 ± 0.10	0.75
22	1.56 ± 0.04	5.25 ± 0.06	7.07	0.12	1.83 ± 0.09	0.92
23	1.53 ± 0.05	5.51 ± 0.07	7.23	0.13	1.99 ± 0.13	1.03
24	1.99 ± 0.07	5.75 ± 0.15	7.94	0.16	1.36 ± 0.10	0.95

^{a} Thermal bremsstrahlung temperature

from the archival database. In addition, we also analysed our *BeppoSAX* data taken in early 2000. Both the LSP and PDM were applied in the same way to search for any periodicity. Fig. 13 shows the results from the LSP for the *ASCA* GIS, *EXOSAT* ME and *BeppoSAX* LECS data. Clearly no period at 4.19 hr is detected. In addition, variability on shorter timescales is not seen in the LSP, which confirms our *RXTE* results described above.

6 DISCUSSION

6.1 Orbital Modulation

We have observed the luminous LMXB GX 9+9 simultaneously with X-ray and optical telescopes. In the optical, the source was seen at $B = 16.96 \pm 0.05$ and $V = 16.79 \pm 0.05$, which is very consistent with previous observations (Schaefer 1990). The high quality optical light curves of GX 9+9 presented here confirm the 4.19-hr periodicity found previously (Schaefer 1990). The stability of this period also shows that it is the orbital period of the system. Unlike in the optical, no significant X-ray modulation on the 4.19 hr period was detected in the four-night *RXTE* observations and other archival X-ray observations (see §5). This is somewhat inconsistent with the previous *HEAO-1* results (Hertz & Wood 1988), in which a 3.8% modulation was found. In fact, the *HEAO-1* data showed large scatter (4.6% residual error) and the light curve was based on 74 data points, typically $\sim$ 1.9 hr apart and spread over 5.91 days. Their detected 4.19 hr X-ray modulation is only marginally significant at the 99% confidence level. Comparing the two observations

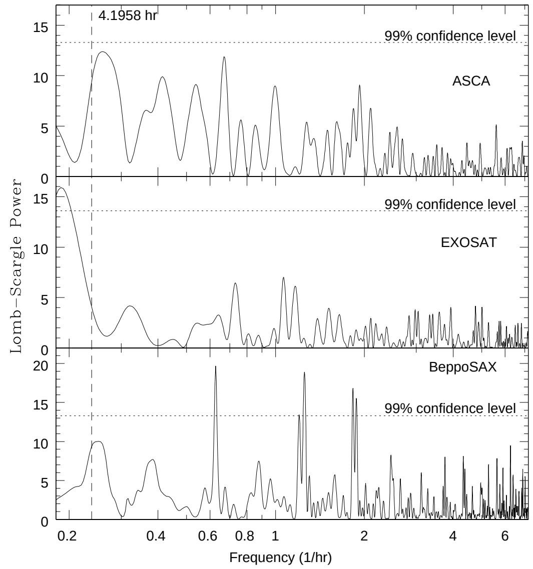

Figure 13. LSP of the *ASCA*, *EXOSAT* and *BeppoSAX* observations of GX 9+9 (see Table 6). The dotted horizontal line is the 99% confidence level, while the vertical dashed line is the 4.19-hr orbital period. No significant peak at the orbital period is seen in either plot. Note that the peaks in the *BeppoSAX* LSP are due to the window function arising from the data gaps, typically seen in low-Earth orbit satellites.

Table 4. Spectral fits of GX 9+9 with the BB+CompST model.

Number	kT_{bb} (keV)	kT_e^a (keV)	τ^b	y^c	F_{tot}	F_{bb}/F_{tot}	R_{bb} (km)	χ^2_ν (34 dof)
1	1.72 ± 0.03	2.95 ± 0.10	11.22 ± 0.52	2.90	8.35	0.17	1.97 ± 0.07	0.69
2	1.50 ± 0.04	3.00 ± 0.13	10.36 ± 0.53	2.50	7.64	0.21	2.69 ± 0.14	0.90
3	1.56 ± 0.03	2.83 ± 0.09	11.22 ± 0.42	2.78	7.86	0.17	2.31 ± 0.09	0.69
4	1.45 ± 0.02	3.11 ± 0.11	9.40 ± 0.34	2.15	7.13	0.22	2.87 ± 0.08	1.17
5	1.45 ± 0.02	3.16 ± 0.09	9.48 ± 0.28	2.22	7.16	0.24	2.98 ± 0.08	0.62
6	1.50 ± 0.02	3.22 ± 0.13	9.27 ± 0.39	2.16	7.46	0.23	2.78 ± 0.07	0.96
7	1.42 ± 0.03	3.06 ± 0.14	9.55 ± 0.48	2.18	6.93	0.20	2.79 ± 0.12	0.88
8	1.43 ± 0.02	3.12 ± 0.09	9.37 ± 0.29	2.14	7.00	0.20	2.81 ± 0.08	0.75
9	1.40 ± 0.02	3.02 ± 0.10	9.75 ± 0.34	2.24	6.94	0.19	2.80 ± 0.08	0.94
10	1.42 ± 0.02	3.00 ± 0.10	9.87 ± 0.37	2.28	7.16	0.23	3.06 ± 0.09	1.13
11	1.37 ± 0.02	3.00 ± 0.08	9.77 ± 0.29	2.24	6.81	0.17	2.80 ± 0.08	0.91
12	1.43 ± 0.02	3.08 ± 0.13	9.51 ± 0.42	2.18	7.23	0.22	2.99 ± 0.09	1.08
13	1.96 ± 0.02	2.81 ± 0.11	12.18 ± 0.68	3.60	8.79	0.10	1.20 ± 0.02	0.87
14	1.74 ± 0.04	2.89 ± 0.09	11.54 ± 0.48	3.00	8.44	0.19	2.04 ± 0.10	0.58
15	1.50 ± 0.03	3.03 ± 0.13	9.97 ± 0.48	2.35	7.49	0.22	2.77 ± 0.11	0.96
16	1.56 ± 0.03	3.03 ± 0.13	10.23 ± 0.52	2.47	7.83	0.24	2.70 ± 0.10	1.32
17	1.72 ± 0.03	3.08 ± 0.14	10.43 ± 0.55	2.62	8.21	0.20	2.10 ± 0.07	0.91
18	1.58 ± 0.03	3.18 ± 0.15	9.73 ± 0.48	2.35	7.59	0.27	2.75 ± 0.10	1.35
19	1.86 ± 0.02	3.20 ± 0.13	10.41 ± 0.48	2.71	8.97	0.23	2.01 ± 0.04	0.86
20	1.87 ± 0.03	3.06 ± 0.11	11.15 ± 0.49	2.97	8.78	0.22	1.93 ± 0.06	0.83
21	1.52 ± 0.04	2.96 ± 0.12	10.46 ± 0.50	2.53	7.71	0.22	2.74 ± 0.15	0.80
22	1.47 ± 0.02	3.12 ± 0.09	9.53 ± 0.30	2.22	7.18	0.23	2.83 ± 0.07	0.82
23	1.47 ± 0.02	3.38 ± 0.16	9.12 ± 0.43	2.20	7.34	0.21	2.76 ± 0.07	1.00
24	1.65 ± 0.05	3.16 ± 0.20	10.27 ± 0.77	2.61	8.04	0.18	2.14 ± 0.13	0.93

[a] Electron temperature of the Comptonizing cloud
[b] Optical depth of the Comptonizing cloud
[c] Comptonization parameter $y = 4kT_e\tau^2/m_ec^2$

from *HEAO-1*, the 4.19-hr X-ray modulation is only found in one of them. Since the source often has flaring and short-term variation (< 1 hr) especially in hard X-rays (> 10 keV; see Fig. 1–4), such activities might cause a false alarm in determining the period and account for the large errors if the time resolution is poor. Hence, these results should be treated with caution. The *RXTE* data and other archival observations reported here provide much higher time resolution and energy-selected light curves to study the 4.19-hr modulation of this source in greater detail. Both LSP and PDM analysis show no indication of variability on this timescale. However, it is possible that an X-ray periodicity might be detectable from time to time as a result of changes in the accretion geometry (such as the height of the disc rim), and it should be noted that the X-ray period was discovered prior to the optical modulation. Consequently, the agreement between the two periodicities means that the original X-ray modulation should not be discarded.

The lack of X-ray modulation and eclipses or absorption dips on the orbital period is common amongst LMXBs and indicates that the inclination angle of the system must be low ($< 70°$). Hertz and Wood (1988) assume that a $1.4 M_\odot$ neutron star is orbiting a low-mass main sequence secondary which is filling its Roche lobe and use the lack of eclipses to show that the inclination of GX 9+9 is less than $\sim 63°$. We also note that the observed semi-amplitude (9.8%) of the optical modulation suggests an orbital inclination of less than 70° (van Paradijs & McClintock 1995). Although the *RXTE* data presented here cannot confirm the X-ray modulation found by Hertz and Wood (1988), the result is still consistent with the hypothesis that GX 9+9 is a low inclination system. In order to account for the small amplitude X-ray variability on the orbital period, Hertz & Wood (1988) suggested that the disc does not hide the central neutron star (since it is at low inclination angle) and instead we are actually observing directly the X-ray emission from the vicinity of the central source. Therefore Hertz & Wood (1988) proposed a variable covering of an accretion disc corona by the edge of the disc. Alternatively, Schaefer (1990) suggested that the X-ray modulation is caused by the changing visibility of X-ray flux reflected off the bright spot although it is more likely that this mechanism could explain the optical modulation.

6.2 The Origin of the Optical Modulation

The observed orbital period of GX 9+9 provides a valuable tool for understanding the system geometry. Assuming a canonical value for the mass of a neutron star ($M_X = 1.4\,M_\odot$), then from Kepler's third law,

$$a = 1.471\,R_\odot (1+q)^{1/3} \tag{1}$$

where a is the separation between the two stars, q is the mass ratio, i.e., M_2/M_X and M_2 is the mass of the companion star. As the companion fills its Roche lobe, the radius of the companion is given by (Paczyński 1971)

Table 5. Spectral fits of GX 9+9 with the BB+CompTT model.

Number	kT_{bb} (keV)	T_0^a (keV)	kT_e (keV)	τ	y	F_{tot}	F_{bb}/F_{tot}	R_{bb} (km)	χ^2_ν (33 dof)
1	1.91 ± 0.03	0.55 ± 0.02	4.12 ± 0.82	7.90 ± 1.54	2.00	8.19	0.34	2.20 ± 0.07	0.62
2	1.64 ± 0.05	0.50 ± 0.03	3.81 ± 0.55	8.38 ± 1.20	2.04	7.51	0.30	2.67 ± 0.16	0.86
3	1.76 ± 0.05	0.53 ± 0.02	3.56 ± 0.51	8.81 ± 1.37	2.16	7.71	0.29	2.31 ± 0.13	0.65
4	1.59 ± 0.03	0.51 ± 0.02	4.26 ± 0.66	7.16 ± 1.00	1.71	6.96	0.30	2.73 ± 0.10	1.00
5	1.58 ± 0.03	0.50 ± 0.02	4.13 ± 0.45	7.58 ± 0.78	1.85	7.01	0.30	2.81 ± 0.10	0.56
6	1.62 ± 0.04	0.50 ± 0.02	4.14 ± 0.70	7.53 ± 1.18	1.83	7.30	0.30	2.73 ± 0.13	0.86
7	1.60 ± 0.04	0.53 ± 0.02	4.61 ± 1.13	6.67 ± 1.44	1.60	6.76	0.30	2.67 ± 0.13	0.64
8	1.57 ± 0.03	0.51 ± 0.02	3.86 ± 0.41	7.81 ± 0.80	1.84	6.83	0.27	2.65 ± 0.10	0.66
9	1.54 ± 0.05	0.50 ± 0.02	3.52 ± 0.41	8.59 ± 1.00	2.03	6.79	0.25	2.63 ± 0.17	0.89
10	1.61 ± 0.03	0.52 ± 0.02	4.48 ± 0.87	6.90 ± 1.20	1.67	7.00	0.31	2.72 ± 0.10	0.79
11	1.52 ± 0.04	0.51 ± 0.02	3.48 ± 0.26	8.62 ± 0.68	2.02	6.66	0.24	2.61 ± 0.14	0.82
12	1.53 ± 0.05	0.49 ± 0.02	3.51 ± 0.40	8.60 ± 1.03	2.03	7.08	0.28	2.88 ± 0.18	0.99
13	2.05 ± 0.03	0.55 ± 0.03	3.88 ± 0.92	8.32 ± 2.09	2.10	8.64	0.34	1.97 ± 0.05	0.77
14	1.90 ± 0.03	0.52 ± 0.02	3.84 ± 0.54	8.55 ± 1.24	2.19	8.30	0.31	2.14 ± 0.07	0.50
15	1.65 ± 0.04	0.52 ± 0.02	4.00 ± 0.71	7.74 ± 1.32	1.87	7.32	0.31	2.64 ± 0.13	0.78
16	1.72 ± 0.03	0.53 ± 0.02	5.00 ± 1.53	6.50 ± 1.69	1.65	7.68	0.36	2.71 ± 0.10	1.14
17	1.90 ± 0.03	0.56 ± 0.02	5.86 ± 2.98	5.76 ± 2.42	1.52	8.03	3.06	2.33 ± 0.07	0.78
18	1.75 ± 0.03	0.53 ± 0.02	10.41 ± 14.95	3.70 ± 4.47	1.11	7.42	0.37	2.61 ± 0.09	0.78
19	1.96 ± 0.03	0.53 ± 0.02	4.74 ± 1.36	7.24 ± 1.85	1.94	8.81	0.38	2.30 ± 0.07	0.79
20	1.99 ± 0.03	0.53 ± 0.02	4.12 ± 0.86	8.26 ± 1.71	2.20	8.64	0.33	2.05 ± 0.06	0.75
21	1.70 ± 0.03	0.52 ± 0.02	4.58 ± 1.03	7.02 ± 1.39	1.76	7.56	0.33	2.65 ± 0.10	0.58
22	1.59 ± 0.03	0.49 ± 0.02	4.14 ± 0.46	7.53 ± 0.76	1.83	7.04	0.30	2.77 ± 0.10	0.70
23	1.64 ± 0.04	0.54 ± 0.02	5.62 ± 1.90	5.98 ± 1.66	1.57	7.17	0.32	2.73 ± 0.13	0.79
24	1.75 ± 0.07	0.49 ± 0.04	3.54 ± 0.51	9.45 ± 1.50	2.47	7.91	0.25	2.22 ± 0.17	0.92

[a] Temperature of seed photons

Table 6. Archival X-ray observations of GX 9+9.

Date	Satellite	Energy Range (keV)	Time span ks / hr	On-source time ks / hr	Remark
1983 Sept 27	*EXOSAT*	0.05–2	62.6 / 17.4	51.7 / 14.4	Nearly uninterrupted
1994 March 25	*ASCA*	0.5–10	47.2 / 13	23.7 / 6.6	
2000 April 8	*BeppoSAX*	0.1–10	100 / 27.8	23.6 / 6.4	

$$R_2 = 0.462a\left(\frac{q}{1+q}\right)^{1/3} \tag{2}$$

From the main-sequence mass-radius relation (Patterson 1984)

$$R_2 = 1.0\,R_\odot\left(\frac{M_2}{M_\odot}\right)^{0.88} = 1.344\,R_\odot q^{0.88} \tag{3}$$

Solving the above three equations simultaneously, we obtain $M_2 = 0.4\,M_\odot,\ R_\odot = 0.45$, $q = 0.29$ and $a = 1.6\,R_\odot$. This corresponds to an early M dwarf (M0 V–M5 V) with a surface temperature of ~ 3400 K and an absolute magnitude $M_V \approx 10$. From the measured V magnitude of 16.79, this gives $M_V = 3$ (assuming a distance of 5 kpc and $A_V = 0.3$). Hence, the observed optical flux is substantially larger than that from the M star itself and it is clear that the optical flux must be due to X-ray reprocessing in the accretion disc and illuminated face of the companion star. There are at least three possible origins of the optical flux and its variation associated with the orbital period: (i) the accretion disc; (ii) the X-ray heating of the companion star which is not in the shadow of the disc; and (iii) the bright spot in the edge of the accretion disc. However, we do not have unambiguous phasing information for this system and it is impossible to determine the variation of these components with respect to orbital phase.

Haswell et al. (2000) proposed that GX 9+9 is a possible persistent superhumper based on the fact that $q \lesssim 0.3$ (based on its short period and compact object mass of at least $1.4 M_\odot$) and also the similarity of the fractional amplitude of the optical modulation to that of superhumps seen in SXTs (O'Donoghue & Charles 1996). Unlike in the case of cataclysmic variables, in which superhumps are caused by a tidally-driven modulation of the disc's viscous dissipation which varies on the beat between the orbital and disc precession period, the optical emission of LMXBs is dominated by X-ray reprocessing. Hence a different mechanism is required to account for the superhump period. A possible solution is to associate the superhumps with varying X-ray reprocessing by changing disc area (Haswell et al. 2000). In other words, the disc surface area varies on the superhump period, resulting in a modulation in the optical emission. If this is the case, we would expect a superhump period which is slightly (a few per cent) longer than the orbital period. However, with the only significant periodicity being that found in the optical (here and earlier work), the lack of an X-ray or spectroscopic modulation still leaves open the possibility that GX 9+9 is a persistent superhumper as the nature of this variation cannot be defined. However, if the X-ray period is true, we can rule out the superhump interpretation.

6.3 Accretion Geometry

The X-ray spectrum of GX 9+9 has rarely been studied in detail even though it belongs to one of the few bright X-ray sources known before *Uhuru* (Bradt et al. 1968). In general, previous studies (e.g. Christian & Swank 1997; Church & Bałucińska-Church 2001) and this work suggest that two-component models are more appropriate in fitting the energy spectrum. Such models consist of a blackbody component plus a Comptonized component (e.g. CPL, TB, CompST and CompTT). Similar behaviour is also found in other high-luminosity LMXBs (White, Stella & Parmar 1988).

The physical interpretation of the origin of such multi-component models is still poorly understood although observations have been made for many LMXBs (e.g., White, Stella & Parmar 1988; Barret et al. 2000; Bloser et al. 2000a; Bloser et al. 2000b). It is widely accepted that the hard component (i.e. the Comptonized component) is due to Comptonization of soft photons in a hot corona, while the source of the soft photons which lead to a Compton up-scattering and the soft thermal component are still the subject of debate (e.g. White, Stella & Parmar 1988). There are several possibilities to explain the origin of the soft thermal component. The most straightforward solution is that this soft component originates from an optically thick accretion disc or an optically thick boundary layer where the accreted matter intersects the neutron star surface. However, Sunyaev & Shakura (1986) showed that the luminosity of the boundary layer should be at least equal to that of the disc if relativistic effects are included, whereas we have found that the BB contribution ranges only from $\sim 10 - 40\%$. In fact, many authors have found similar results for other sources (White, Stella & Parmar 1988; Barret et al. 2000; Bloser et al. 2000a; Bloser et al. 2000b). Therefore Guainazzi et al. (1998) and Barret et al. (2000) suggest that the weak thermal component could be due to an optically thick accretion disc, while the other Comptonized component arises from an optically thin boundary layer. However, this picture is not suitable to explain the similarities in spectral behaviour between neutron stars and black holes since a black hole does not have a physical surface (see Barret et al. 2000). Moreover, the negative result from the DBB model also suggests that the soft component might not be from the inner accretion disc, and such a model is not a good description of the *RXTE* data presented here. Therefore the Comptonized component is unlikely to be due to the boundary layer and such a disc corona model can likely be ruled out.

Among several models mentioned here, the present data are more consistent with a picture in which the soft component is produced by an optically *thick* boundary layer while the hard component is from an extended hot corona. As discussed above, such a model cannot explain the small contribution of the blackbody emission. Hence some mechanism should suppress the boundary layer emission relative to that of the corona and disc. One possibility is that the rotation period of the neutron star is close to equilibrium with the Keplerian period of the inner edge of the accretion disc (White, Stella & Parmar 1988) such that little energy is given up in the boundary layer. Another possibility is that part of the boundary layer emission is blocked by the inner disc corona or thickened disc (Lamb 1986; van der Klis et al. 1987). Such mechanisms have been discussed for the X-ray spectrum of 4U 1916–05 (Church et al. 1998; Bloser et al. 2000a). In particular, Bloser et al. (2000a) have shown that by fitting a BB+CPL model, the blackbody radius of 4U 1916–05 decreases slightly as the accretion rate increases. In Fig. 12, all four models show a decreasing trend for R_{bb} as the total flux increases. This may indicate that the inner disc can become thicker as the accretion increases and thereby obscure a larger region of the boundary layer. In addition, the derived R_{bb} here is consistent with $\sim$ 2–3 km, implying that the blackbody component can come from only a limited region of the neutron star surface such as an optically thick boundary layer. It is also interesting to note that GX 9+1 (White et al. 1986), 4U 1735–444 (Seon et al. 1997) and 4U 1820–30 (Bloser et al. 2000b), which are all luminous atoll sources, show similar blackbody radii in the persistent spectrum. Spectral analysis of these sources also suggests that the blackbody component comes from an optically thick boundary layer.

Applying the above accretion geometry to describe GX 9+9, one would expect to detect an iron K emission line at 6.4–6.7 keV which is a common feature of the spectra of many luminous LMXBs (e.g. White et al. 1986; Barret et al. 2000), as a result of the accretion disc corona (see Fabian, Guilbert & Ross 1982). However, observations have shown that such emission is not present in GX 9+9 (see Church & Bałucińska-Church 2001). Interestingly, GX 9+1 is also well-known for its lack of iron K emission (White et al. 1986). A reflection model (*pexrav* in `XSPEC`) was also used to fit the spectra so as to search for a reflection component from the disc, but the derived reflection factor was consistent with zero and thus there is no evidence of reflection. One possible reason for this is the relatively low corona temperature such that the hard photons from the corona will tend to be photoelectrically absorbed by the matter in the disc, rather than Compton scattered. The lack of the line emission and reflection component indicates that a significant fraction of the disc cannot be seen, either by reflection or irradiation.

Regarding a physical interpretation of the spectral models, a thermal bremsstrahlung interpretation for the hard component seems to be unrealistic since the derived radius of the plasma cloud is too far from the neutron star ($\sim 10^9$ cm) to be heated to several keV by the neutron star (White et al. 1986). On the other hand, although the CompTT model is an improved version of CompST which includes relativistic effects and extends to the cases of both optically thin and thick plasmas, the larger error bars of optical depth and electron temperature compared to CompST make the CompST model more suitable to describe the present *RXTE* data. Therefore, we will refer to the CompST model when discussing Comptonization below. For the CPL model, it approximates an unsaturated Comptonized spectrum ($y = 4kT_e\tau^2/m_ec^2 \approx 1$) of cool photons up-scattered in a hot electron plasma and its results may not be directly interpretable in terms of a physical description. Therefore the CompST model can give a more complete description of the source spectrum. In fact, several luminous X-ray sources (such as 4U 1636–536, 4U 1820–30, Sco X–1, Sco X–2, Cyg X–2, GX 9+1 and GX 17+2) have shown that the CompST and CPL models provide equally good fits to the source spectrum (Christian & Swank 1997). It is also interesting to note that the derived kT_e and τ for Sco X–1, 4U 1735-444, 4U 1916–05, 4U 1820–30, Cyg X–2, GX 9+1, GX 17+2 and KS 1731–260 are very similar to the results presented here (see Table 7).

The high-quality *RXTE* data presented here can be summarised with the following physical model: in the upper banana state, the luminosity is relatively high and the blackbody radiation comes from an optically thick boundary layer which is partly obscured by the inner accretion disc, producing $\sim$ 10–40% blackbody flux from a small equatorial region of the neutron star. Increases in the blackbody flux are also responsible for the flaring activity. Similar behaviour is also found in Sco X–1 (White, Peacock & Taylor 1985) and Sco X–2 (White et al. 1986). A hot electron cloud ($T \approx 3.5 \times 10^7$ K) in the form of an accretion disc corona surrounds the neutron star and at such high luminosity, the blackbody photons from the boundary layer can heat up the corona to maintain its temperature (see Fig. 12) at about a constant level in spite of the Compton cooling. The relatively strong blackbody radiation produces more extensive ionisation and hence increases the optical depth τ of the corona, reducing the radiation drag that generates QPOs in the framework of the sonic-point model (Miller, Lamb & Psaltis 1998), and thereby accounting for the lack of kHz QPO in GX 9+9. It is also known that when other atoll sources (e.g. 4U 1636–53: Wijnands et al. 1997; 4U 1820–30: Smale, Zhang & White 1997) are in their upper banana branch, kHz QPOs do not occur.

7 CONCLUSIONS

Simultaneous *RXTE* and optical high-speed observations were performed to study the atoll source GX 9+9. The high-quality optical light curves from high-speed CCD photometry during a four-night observation confirm, but with much greater precision, the 4.19-hr orbital period (Schaefer 1990). However, our *RXTE* observations cannot confirm the X-ray modulation at the orbital period (Hertz & Wood 1988). By using archival *ASCA* and *EXOSAT* data, and also our recent *BeppoSAX* observation, no X-ray modulation could be revealed. GX 9+9 also shows variability on timescales $\sim$ 1.4 hr in the optical light curves which could be related to the mHz QPO as seen in other LMXBs. We do not find any significant X-ray/optical correlation in the light curves. Observations indicate that the inclination angle of GX 9+9 cannot be too high ($< 70^\circ$). The observed optical flux is mainly due to X-ray irradiation of the outer accretion disc and the reprocessing of a bright spot in the disc and X-ray heating of the companion can contribute the observed modulation. The CD and HID show that GX 9+9 was in the upper banana state during observations. Time-resolved X-ray spectroscopy was also performed and several two-component spectral models (BB+CPL, BB+TB, BB+CompST and CompTT) can provide a good fit to the energy spectra. A two-component spectral model is always required to fit the X-ray emission from several luminous LMXBs (see Table 7). In general, such models consist of a blackbody component (soft component) and a Comptonized component (hard component). The blackbody component is often interpreted as the contribution from either an optically thick accretion disc or an optically thick boundary layer (interaction between the inner accretion disc and the neutron star's surface). On the other hand, the hard component may be from a hot extended corona, optically thin boundary layer. The likely interpretation for GX 9+9 can be understood in terms of an optically thick boundary layer (soft component) which is partly obscured by the inner disc or thickened disc, while the hard Comptonized component is from an extended hot corona.

ACKNOWLEDGMENTS

We thank Christine Done for the red-noise generator code, and the *RXTE* SOC team for their efforts in schuduling the simultaneous observations.

REFERENCES

Barret D., Olive J. F., Boirin L., Done C., Skinner G. K., Grindlay J. E., 2000, ApJ, 533, 329.

Berendsen S. G. H., Fender R., Kuulkers E., Heise J., van der Klis M., 2000, MNRAS, 318, 599.

Bloser P. F., Grindlay J. E., Karret P., Zhang W., Smale A. P., Barret D., 2000a, ApJ, 542, 1000.

Bloser P. F., Grindlay J. E., Barret D., Boirin L., 2000b, ApJ, 542, 989.

Bradt H., Naranan S., Rappaport S., Spada G., 1968, ApJ, 152, 1005.

Bradt H. V., Rothschild R. E., Swank J. H., 1993, ApJSS, 97, 355.

Chakrabarty, D., Homer, L., Charles, P. A., & O'Donoghue, D. 2001, ApJ, 562, 985

Charles P. A., Thorstensen J. R., Bowyer S., 1977, IAU Circ, 3096.

Christian D. J., Swank J. H., 1997, ApJSS, 109, 177.

Church M. J., Bałucińska-Church M, 2001, A&A, 369, 915.

Church M. J., Parmar A. N., Bałucińska-Church M., Oosterbroek T., Dal Fiume D., Orlandini M., 1998, A&A, 338, 556.

Davidsen A., Malina R., Bowyer S., 1976, A&A, 203, 448.

Done C., Madejski G. M., Mushotzky R. F., Turner T. J., Koyama K., Kunieda H., 1992, ApJ, 400, 138.

Dove J. B., Wilms J., Nowak M. A., Vaughan B. A., Begelman M. C., 1998, MNRAS, 298, 729.

Table 7. BB+CompST spectral fits of other luminous LMXBs.

Source	kT_{bb} (keV)	kT_e (keV)	τ	Reference
Sco X–1	1.6	3	10.5	White, Peacock & Taylor 1985
4U 1735–444	1.45–1.90	3.05–3.26	11.93–13.99	Seon et al. 1997
4U 1916–05^a	1.49–2.03	3.53–8.85	5.78–13.46	Bloser et al. 2000a
4U 1820–30^a	1.30–2.36	2.75–7.94	6.00–15.21	Bloser et al. 2000b
Cyg X–2	1.13	3.75	8.4	Christian & Swank 1997
GX 9+1	1.49	3.00	10.9	White, Stella & Parmar 1988
GX 17+2	1.18	3.00	13.0	White, Stella & Parmar 1988
KS 1731–260	1.00–1.30	2.60–2.80	10.40–12.60	Barret et al. 2000
GX 9+9	1.37–1.96	2.81–3.38	9.12–12.18	this work

^{a} Use CompTT instead of CompST for the Comptonized component

Fabian A. C., Guilbert P. W., Ross R. R., 1982, MNRAS, 199, 1045.

Guainazzi M., Parmar A. N., Segreto A., Stella L., Dal Fiume D., Oosterbroek T., 1998, A&A, 339, 802.

Haswell C. A., King A. R., Murray J. R., Charles P. A., 2000, MNRAS, 321, 475.

Hertz P., Wood K. S., 1988, ApJ, 331, 764.

Homer L., Charles P. A., O'Donoghue D., 1998, MNRAS, 298, 497.

Kong A. K. H., Homer L., Kuulkers E., Charles P. A., Smale A. P., 2000, MNRAS, 311, 405.

Kong A. K. H., 2000, *PhD thesis*, University of Oxford.

Lamb F. K., 1986. In: *The Evolution of X-Ray Binaries*, p. 151, eds Trümper J., Lewin W. H. G., Brinkman W., Dordrecht: Reidel.

Mason K. O., Charles P. A., White N. E., Culhane J. L., Sanford P. W., Strong K. T., 1976, MNRAS, 177, 513.

Miller M. C., Lamb F. K., Psaltis D., 1998, ApJ, 508, 791.

Mitsuda K., Inoue H., Koyama K. et al., 1984, PASJ, 36, 741.

O'Donoghue D., 1995. *Baltic Astronomy*, 4, 519.

O'Donoghue, D. & Charles, P. A. 1996, MNRAS, 282, 191.

Paczyński B., 1971, ARA&A, 9, 183.

Parsignault D. R., Grindlay J. E., 1978, ApJ, 225, 970.

Patterson J., 1984, ApJSS, 54, 443.

Predehl P., Schmitt J. H. M. M., 1995, A&A, 293, 889.

Schaefer B. E., 1990, ApJ, 354, 720.

Schild R. E., 1977, AJ, 82, 337.

Schulz N. S., Hasinger G., Trümper J., 1989, A&A, 225, 48.

Schulz N. S., 1999, ApJ, 511, 304.

Seon K.-I., Min K.-W., Yoshida K., Makino F., Lewin W. H. G., van der Klis M., van Paradijs J., 1997, ApJ, 479, 398.

Shahbaz T., Smale A. P., Charles P. A., van Paradijs J., Hassall B. J. M., Callanan P., 1996, MNRAS, 282, 1437.

Smale A. P., Zhang W., White N. E., 1997, ApJL, 483, 119.

Stellingwerf R. F., 1978, ApJ, 224, 953.

Sunyaev R. A., Shakura N. I., 1986, Sov. Astron. Lett., 12, 117.

Sunyaev R. A., Titarchuk L. G., 1980, A&A, 86, 121.

Timmer J., König M., 1995, A&A, 300, 707.

Titarchuk L., 1994. ApJ, 434, 570.

van der Klis M. K., Stella L., White N., Jensen F., Parmar A. N., 1987, ApJ, 316, 411.

van Paradijs J., McClintock J. E., 1995, In: *X-ray Binaries*, p. 58, eds Lewin W. H. G., van Paradijs J., van den Heuvel E. P. J., Cambridge Univ. Press, Cambridge.

Vrtilek S. D., Penninx W., Raymond J. C., Verbunt F., Hertz P., Wood K., Lewin W. H. G., Mitsuda K., 1991, ApJ, 376, 278.

White N. E., Peacock A., Hasinger G., Mason K. O., Manzo G., Taylor B. G., Branduardi-Raymont G., 1986, MNRAS, 218, 129.

White N. E., Peacock A., Taylor B. G., 1985, ApJ, 296, 475.

White N. E., Stella L., Parmar A. N., 1988, ApJ, 324, 363.

Wijnands R. A. D., van der Klis M., van Paradijs J., Lewin W. H. G., Lamb F. K., Vaughan B., Kuulkers E., 1997, ApJL, 479, 141.

Wijnands R., van der Klis M., van Paradijs J., 1998. In: *IAU Sumposium 188 "The Hot Universe"*, p. 370, eds Koyama K., Kitamoto S., Itoh M., Dordrecht: Kluwer Academic.

Wilms J., Nowak M. A., Dove J. B., Fender R. P., di Matteo T., 1999, ApJ, 522, 460.